AAAS
Energy Material Advances
Volume 2021, Article ID 9795825, 11 pages
https://doi.org/10.34133/2021/9795825

Energy Material Advances
A SCIENCE PARTNER JOURNAL

Research Article

Sodium-Ion Battery Anode Construction with SnP_x Crystal Domain in Amorphous Phosphorus Matrix

Baixu Chen,[1,2,3] Yubo Yang,[1,2] Aibing Chen,[3] Xu Zhang,[1,2] Jaffer Saddique,[1,2,4] Mingxue Tang,[5] and Haijun Yu[1,2]

[1]*Institute of Advanced Battery Materials and Devices, College of Materials and Manufacturing, Beijing University of Technology, Beijing 100124, China*
[2]*Key Laboratory of Advanced Functional Materials, Ministry of Education, Beijing University of Technology, Beijing 100124, China*
[3]*College of Chemical and Pharmaceutical Engineering, Hebei University of Science and Technology, Shijiazhuang 050018, China*
[4]*College of Materials Science & Technology, Jiangsu Key Laboratory of Materials and Technology for Energy Conversion, Nanjing University of Aeronautics & Astronautics, Nanjing 210016, China*
[5]*Center for High Pressure Science & Technology Advanced Research, Beijing 100094, China*

Correspondence should be addressed to Aibing Chen; chen_ab@163.com, Xu Zhang; zhangx@bjut.edu.cn, and Haijun Yu; hj-yu@bjut.edu.cn

Received 11 March 2021; Accepted 23 August 2021; Published 1 October 2021

The high-capacity phosphorus- (P-) based anode materials for sodium-ion batteries (NIBs) often face poor performance retentions owing to the low conductivity and large volume expansion. It is thus essential to buffer these problems by appropriately alloying with other elements such as tin (Sn) and constructing well-designed microstructures. Herein, a series of P-/Sn-based composites have been synthesized by the facile and low-cost one-step ball milling. Pair distribution function (PDF) has been employed as a hardcore quantitative technique to elucidate their structures combined with other techniques, suggesting the formation and ratios of Sn_4P_3 and Sn crystalline domains embedded inside an amorphous P/carbon matrix. The composite with the largest amount of Sn_4P_3 in the P/C matrix can deliver the most balanced electrochemical performance, with a capacity of 422.3 mA-h g^{-1} for 300 cycles at a current density of 1000 mA g^{-1}. The reaction mechanism has been elucidated by ^{23}Na and ^{31}P solid-state nuclear magnetic resonance (NMR) investigations. The study sheds light on the rational design and concrete identification of P-/Sn-based amorphous-dominant composite materials for NIBs.

1. Introduction

Sodium-ion batteries (NIBs) are expected to be a vital alternative to the extensively used lithium-ion batteries (LIBs) by considering the high abundance and low cost of sodium resources [1–4]. On the survey of electrode materials for NIBs, phosphorus (P) and tin (Sn) have gained wide attentions as anode materials because of their high theoretical capacities, low discharge voltages, and low costs. However, both of them suffer from large volume expansions when alloying with Na, leading to the structural collapse, particle pulverization, electrochemical separation of active materials, and thus rapid performance decay [5, 6]. Moreover, the nonmetallic P and phosphides have poor conductivities, while the metallic Sn and its sodiation products can easily aggregate; both effects significantly reduce the electrochemical efficiency of NIBs [7–10]. It has been demonstrated that the cooperation of P and Sn, through either physical incorporation or chemical alloying, can attenuate the intrinsic drawbacks of individual P or Sn. Particularly, the compound Sn_4P_3 has been shown an appealing anode material for NIBs because of the synergetic electrochemistry of P and Sn elements [7, 11–14]. Still, the elegant design of P/Sn composite anode materials, in terms of the chemical component, ratio, crystallinity, sizes, distribution, uniformity, interface, etc., is essential to further optimize the overall performance in NIBs [11, 15–18].

To synthesize high-performance P-/Sn-based anode materials, many approaches have been employed, such as high-energy ball milling (HEBM) [19, 20], construction of

yolk-shell spheres [21–24], and hydrothermal synthesis of heterostructures [25]. Among them, HEBM is of excellent practicability owing to its low cost, easy scale-up, and little reaction media involved [26, 27]. However, the precise control of P-/Sn-based composite structures by HEBM, often combining carbon materials to improve the conductivity, is challenging because of the complicate and inhomogeneous mechanochemical reactions between P and Sn, which generate diverse components including P, Sn, and SnP_x with complex structural ordering states [28]. Mulder's group [26] has fabricated a high-rate and stable Sn_4P_3-P@graphene nanocomposite from red P and Sn with a molar ratio of 3 : 1 by a three-stepped HEBM method for NIBs. However, the roles of the P/Sn ratio on the composition and microstructures of the P-/Sn-based composites and subsequent electrochemical performance in NIBs have not been studied. Therefore, it is essential to rationalize the components and microstructures of the P-/Sn-based composites, especially by the P/Sn ratio, to further optimize the performance.

The P-/Sn-based composite materials possess poor long-range ordering, and thus, their elegant structural identification, in terms of components, ratios, localized structures, etc., can hardly be well elucidated by characterizations such as X-ray diffraction (XRD) and transmission electron microscope (TEM). Therefore, it is required to develop new technologies for the structural investigation and quantification. The pair distribution function (PDF) is a powerful characterization technique, which can not only provide local structure information for complicated systems but also quantify the components in ordered or even disordered materials [29–33]. However, owing to the light weight of P, PDF has rarely been used in P-/Sn-based anode materials, making the further structural transformation and reaction mechanism indistinct [13, 34]. Therefore, further attempts on the identification and quantification of microstructures, by means of new characterizations such as PDF, as well as the subsequent mechanism studies, are strongly required for P-/Sn-based anode materials.

In this work, a series of P-/Sn-based composite anode materials have been prepared by a one-step HEBM to rationalize the P/Sn ratios and the resultant microstructures for the optimization of electrochemical performance in NIBs. PDF has been employed as a hardcore quantitative technique to elucidate the structures of these materials, suggesting the formation of Sn_4P_3 and Sn crystalline domains embedded inside amorphous P/carbon matrices with adjustable compositions. It was found that the P-excess composite with the largest amount of crystalline Sn_4P_3 in the P/C matrix can deliver the best overall electrochemical performance. Based on the derived structural information, the reaction mechanism of the optimal anode material has been elucidated by ^{23}Na and ^{31}P solid-state nuclear magnetic resonance (NMR) investigations.

2. Materials and Methods

2.1. Material Preparation. The composite anode materials, including C1, C2, C3, C4, C5, and C6, were prepared by the one-step HEBM of red phosphorous (P), tin (Sn), and super P (C) in different proportions, as listed in Table 1. In detail, raw materials in a certain ratio were transferred into a Wolfram carbide container with 10 mm and 1 mm Wolfram carbide milling balls inside an argon glovebox (H_2O and O_2 contents < 0:1 ppm). The ball-to-material ratio was kept constant to be 40 : 1. The milling container was then transferred from the glovebox into the ball miller. For all composites, the HEBM was carried out at 600 rpm for 12 h valid milling time. After the milling, the container was disassembled inside the glovebox, and the obtained composite anode was collected and sealed before use.

2.2. Electrode Preparation and Electrochemical Measurements. Half-cells were assembled to evaluate the electrochemical performance of all composites. For a typical electrode, a mixture of 80 wt.% active composite and 10 wt.% super P carbon as the conductive additive was prepared by hand milling in an agate crucible for 0.5 h, which was then added with 10 wt.% polyacrylic acid (PAA) solution and stirred for 8 h to get a homogenous slurry. A copper foil was uniformly covered with the obtained slurry by a scraper and dried inside a vacuum oven at 80 °C overnight. The mass loading of the active material was ~1.0 mg cm^{-2}. Finally, the electrode was then cut into small circular sheets and compressed at 10 MPa.

R2032-type coin cells (MTI Co.) were assembled in argon glove box by using the prepared sheets as the working electrode, sodium foil as the counter electrode, and Whatman paper as the separator. A solution of 1.0 mol L^{-1} $NaPF_6$ in propylene carbonate (PC) with 5 vol.% fluoroethylene carbonate (FEC) was used as the electrolyte. The electrochemical performances of all synthesized materials were tested at 25 °C by Neware Test System in the voltage range of 0.01~3.0 V (vs. Na^+/Na). The specific capacity was calculated based on the active composited material. Cyclic voltammetry (CV) was performed in a coin cell using a CHI600c electrochemical work station (Chen Hua Instrument Co., China). Galvanostatic intermittent titration technique (GITT) was performed by Neware Test System with constant current pulse for 1 h and followed relaxation for 2 h to allow the system to reach the electrochemical equilibrium. Full cells were assembled by coupling the representative C3 anode with $Na_3V_2(PO_4)_3$ cathode in the R2032-type coin cell configuration and tested at 25 °C by Neware Test System. The preparation of the cathode electrode is the same as that of the anode electrode, except that the binder uses polyvinylidene fluoride, collector uses aluminum foil, and the conducting carbon uses acetylene black.

2.3. Material Characterization. The crystal structures of all composites were characterized by XRD (Bruker, D8 Discover) with Cu Kα radiation ($\lambda = 0.154$ nm). The morphologies were studied using scanning electron microscopy (SEM) (FEI, Quanta 650) and TEM (JOEL, JEM-2010). Energy-dispersive spectroscopy (EDS) was carried out to evaluate the distribution of elements in the composite anodes. *Ex situ* X-ray photoelectron spectroscopy (XPS, Thermo Scientific ESCALAB 250Xi) was used to investigate the chemical structures of C3 at different electrochemical states.

Table 1: The P/Sn ratios and synthesis conditions for synthesizing composites C1-C6.

Sample	Red P (wt.%)	Sn (wt.%)	C (wt.%)	P/Sn molar ratio	Rotating speed (rpm)	Milling time (h)
C1	10	60	30	0.66	600	12
C2	20	50	30	1.53	600	12
C3	30	40	30	2.87	600	12
C4	40	30	30	5.11	600	12
C5	50	20	30	9.57	600	12
C6	60	10	30	22.97	600	12

^{23}Na and ^{31}P NMR was employed to study the mechanism of the sodiation/desodiation process, which were acquired on a Bruker 400 MHz spectrometer (AVANCE HD III, Germany) with 4.0 mm HX MAS probe. The Larmor frequencies of ^{23}Na and ^{31}P were 105.85 and 162.0 MHz, respectively. All the studied electrodes were filled into 4.0 mm rotors inside an argon glovebox. The spinning rate was set to be 8 kHz. Single pulses of 1.4 and 0.95 μs were set for 90 degree to polarized ^{23}Na and ^{31}P magnetization, respectively. Total 1024 scans were recorded for each measurement to get reasonable signal-to-noise (S/N) ratio. ^{23}Na was externally referenced to a 1 mol L^{-1} NaCl solution at 0 ppm, and the peak of 85 wt.% $H_3PO_{4(aq)}$ at 0 ppm was set as the ^{31}P spectral reference.

High-energy synchrotron total scattering measurements were carried out at the 11-ID-C beamline of the Advanced Photon Source (APS), Argonne National Laboratory. The wavelength of the X-ray is 0.1173 nm. Experimental geometries were calibrated using the CeO_2 powder sample and Fit2D [35] freeware. Fit2D was also used to integrate collected 2D data. The PDF was calculated by a Fourier transform using PDFgetX3 [36] from the integrated data with Qmax up to 27 Å^{-1}. PDFgui [37] was used to simulate PDFs and to fit data of the structures.

3. Results and Discussion

A series of P-/Sn-based composite materials with different compositions and crystalline phases have been prepared by HEBM of red P and Sn (total 70 wt.%) in different ratios together with super P carbon (30 wt.%) (Table 1), which are termed as C1, C2, C3, C4, C5, and C6 with the increased content of red P. The XRD patterns in Figure 1(a) show that C1, C2, and C3 contain crystalline phases, while C4, C5, and C6 only contain amorphous structures. Although the P/Sn molar ratio in C1 (0.66) is close to the stoichiometric P/Sn ratio in Sn_4P_3 (0.75), only the Sn pattern could be identified (Figure 1(b)), which implies that the mechanically generated SnP_x alloys, if any, are dominantly amorphous. With the increase of P/Sn molar ratio to 1.53 in C2 (Figure 1(c)), the Sn pattern becomes noticeably weaker, while a new Sn_4P_3 structure appears, indicating more Sn undergoes mechanochemical alloying with red P. When the P/Sn molar ratio is further increased to 2.87 in C3 (Figure 1(d)), the Sn pattern disappears, while the Sn_4P_3 pattern strengthens, suggesting nearly all Sn has been consumed in the alloying reaction with red P. The absence of observable XRD peaks in C4-C6 suggests the contents of crystalline Sn_4P_3 were ultralow owing to the large excess of amorphous P.

Although the crystalline phases in C1-C3 have been shown by XRD, much information about nanocrystallites as well as amorphous structures can hardly be revealed. In addition, the noncrystalline structures reduce the signal-to-noise (S/N) ratios of XRD patterns, making them less reliable. PDF analysis based on synchrotronic total scattering experiments is powerful to provide atomic structure information for crystalline and disordered materials [32, 33, 38]. We further performed PDF analysis on the prepared materials. As shown in Figure 2(a), regular peaks can be seen for C1-C3, indicating the existence of ordered structures. In contrast, no noticeable peak above 5 Å is observable for C4-C6, suggesting their dominant disordered features.

More detailed structural information can be extracted by fitting the PDF curves based on the crystal structures of Sn and Sn_4P_3. The structural model of Sn in Figure 2(b) displays a tetragonal structure (space group: $I4_1$), with representative Sn-Sn bonds having distances of 3.03 Å ($(Sn\text{-}Sn)_1$) and 4.43 Å ($(Sn\text{-}Sn)_2$) [34]. Similarly, the structural model of Sn_4P_3 in Figure 2(c) displays a trigonal structure (space group: $R\bar{3}m$), with representative bonds having distances of 3.95 Å ($(Sn\text{-}Sn)_3$), 3.95 Å (P-P), and 2.61 Å (Sn-P) [13]. Note the $(Sn\text{-}Sn)_3$ bond has the same distance as the P-P bond in Sn_4P_3. All these peaks can be identified in C1, C2, and C3 in Figure 2(d), suggesting the existence of Sn and Sn_4P_3 alloys. With the decrease of Sn elemental contents from C1, C2, to C3, the intensities of $(Sn\text{-}Sn)_1$ and $(Sn\text{-}Sn)_2$ bonds from the metallic Sn become weaker, in line with the further alloying of Sn crystallites with P when more P was added. In contrast, the intensities of $(Sn\text{-}Sn)_3$/P-P and Sn-P become stronger from C1, C2, to C3, which demonstrates the formation tendency of Sn_4P_3 with the increase of P. Based on the metallic Sn and Sn_4P_3 models, the PDF curves of C1, C2, and C3 can be well fitted, providing quantitative information about the components in these materials. The crystalline Sn/Sn_4P_3 mass ratios in C1, C2, and C3 are calculated to be 94 : 6, 37 : 63, and 2 : 98, respectively.

To investigate the localized structures of the P-/Sn-based anode materials, the representative composite C3 was examined by high-resolution transmission electron microscopy (HRTEM) (Figures 3(a)–3(c)) as well as SEM. The SEM image (Figure S1, supporting information (SI)) shows the agglomerated C3 with irregular shapes comprised of micrometer-sized particles. As shown in the inset of

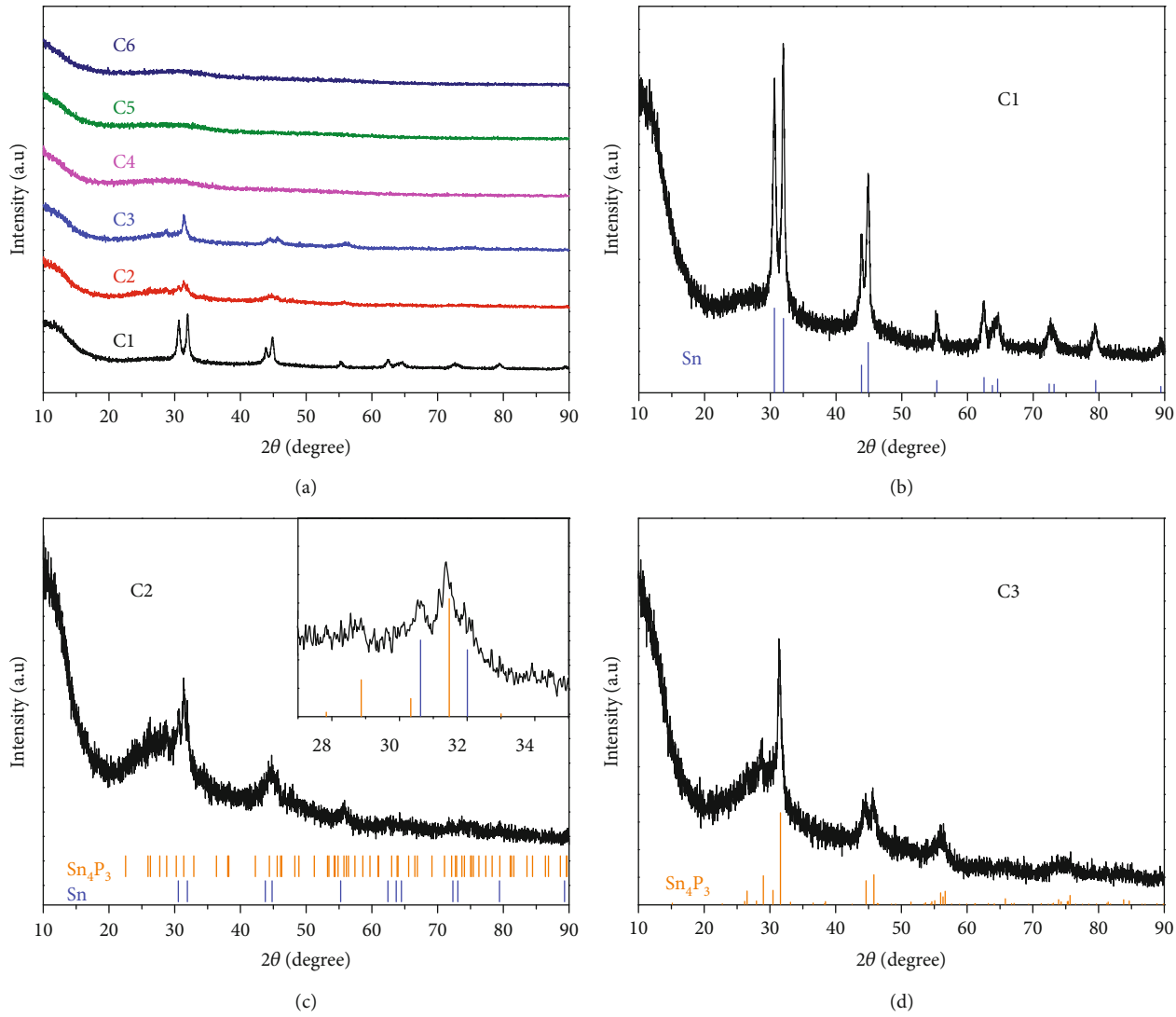

Figure 1: (a) XRD analysis of P-/Sn-based composites C1-C6. (b–d) XRD patterns of C1 (b), C2 (c), and C3 (d). The inset in (c) shows the partially enlarged pattern.

Figure 3(a), C3 displays relatively continuous distribution with dim boundaries, which suggests the dispersive distribution of diverse components after HEBM. The HRTEM image of C3 in Figure 3(a) shows an amorphous master matrix with intimately imbedded crystallites of ~10 nm. The two embedded crystallites are identified to be Sn_4P_3 and Sn according to their lattice fringes with interplanar spacings, as illustrated in the enlarged images in Figures 3(b) and 3(c), respectively. The amorphous matrix is likely composed of amorphous P and carbons. The EDS elemental maps in Figures 3(d)–3(g) reveal that P, Sn, and C are relatively homogeneously distributed in C3, suggesting that Sn_4P_3 and metallic Sn crystalline nanoparticles are nearly evenly distributed in the amorphous matrix.

Such a configuration with nanosized crystal domains diffusely imbedded in a conductive amorphous matrix can combine the effective ion/electron transfer in metallic/-semimetallic crystallites, and the isotropic volume variations of amorphous structures, which will synergistically improve the electrochemical efficiency, mitigate the volume change, and improve the stability. Also, the amorphous P can separate the metallic/semimetallic crystal domains from aggregation, while the amorphous carbon improves the electron conductivity of the composite [28]. The continuous amorphous matrix can also promote the uniform formation of charge/discharge products by tuning the nucleation process [39]. Moreover, one component in the composite may attenuate the volume change, inherent stress, and mechanical instability of another component because of their asynchronous and distinct reactions [40]. With the elegant synergy of crystalline and amorphous structures, composite C3 is expected to deliver better electrochemical performance than that of the all-crystalline or all-amorphous P-/Sn-based anode materials.

The electrochemical performance of these composite anode materials has been evaluated in half-cell NIBs (Figure 4). As shown in the CV curves of the representative

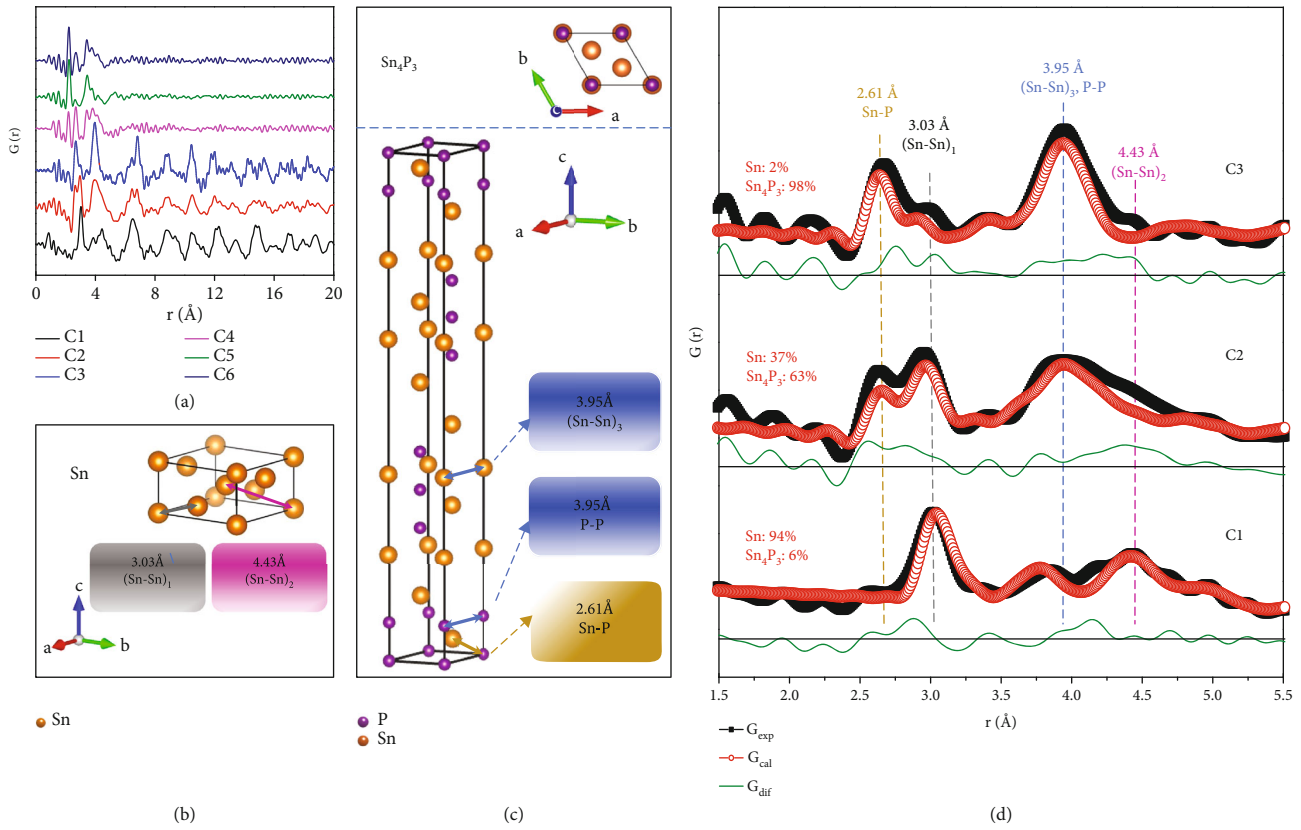

FIGURE 2: The structures of P-/Sn-based materials as probed by PDF. (a) The PDF results of C1-C6. (b, c) The crystal structure models of Sn (b) and Sn_4P_3 (c). The purple and yellow balls represent P and Sn atoms, respectively. The distances of representative bonds are also displayed. (d) A PDF comparison of C1, C2, and C3 based on peak fitting. The blue dot, red, and green curves stand for the experimental pattern, the calculated patterns, and the fitting difference, respectively.

C3 in Figure 4(a), an irreversible broad cathodic peak at ~1.0 V appears in the first sodiation process, which could be attributed to the electrochemical decomposition of the electrolyte and the formation of a solid electrolyte interphase (SEI) film [41]. During the sodiation process, Na^+ ions insert into the C3 composite through the multistep alloying process to form Na-P and Na-Sn species, with the final reaction products to be Na_3P and $Na_{15}Sn_4$, respectively [19, 42]. In the anodic scan, two peaks at 0.4 V and 0.7 V in the first cycle correspond to the two-step desodiation processes that Na^+ ions extract from the Na-P and Na-Sn alloys [14]. The CV curves become almost constant from the second cycle, suggesting the good reversibility of the electrochemical conversions of C3 after its initial stabilization.

The effect of the P/Sn ratio on the electrochemical performance was studied, showing that a balanced P/Sn ratio, i.e., a rational structure comprised of crystal domains embedded in the amorphous matrix, is critical to obtain the optimal performance. As shown in Figure S2, C1 and C2 exhibit stable cycle performance, but the capacities are low because of the high ratios of Sn. On the contrary, owing to the large content of the high-capacity P, C6 has the highest specific capacity but decays rapidly. Similarly, C4 and C5 exhibit poor capacity retention in NIBs. Therefore, the most balanced electrochemical performance with both high capacity and cycling stability could be realized in the C3 composite.

The electrochemical performance of C3 was thus carefully evaluated. GITT was performed to investigate the kinetic behavior of C3, as shown in Figure S3. The diffusion coefficient of Na^+ (D_{Na+}) can be estimated based on Fick's second law according to the equation in SI. The D_{Na+} of C3 maintains a relatively stable level with an order of about 10^{-16}-10^{-15} cm^2 s^{-1} during cycling. Figure 4(b) shows that C3 can deliver a high capacity of 996.8 mA-h g^{-1} at a current density of 200 mA g^{-1}. Note that super P carbon can deliver a capacity of only ~75 mA-h g^{-1} in NIBs at 1 A g^{-1} (Figure S4), suggesting the minor capacity contribution from the carbon component in C3. The rate performance and the corresponding charge/discharge curves of C3 have been tested between 0.01 V and 3.0 V at current densities ranging from 50 to 2000 mA g^{-1} (Figures 4(c) and 4(d)). At current densities of 50, 100, 200, 500, 1000, and 2000 mA g^{-1}, C3 exhibits specific discharge capacity of 1009.4, 923.2, 847.3, 682.6, 607.7, and 493.7 mA-h g^{-1}, respectively. Moreover, when the current density was returned to 50 mA g^{-1}, the discharge capacity could largely recover to 947.2 mAh g^{-1}. The good rate performance demonstrates that C3 favors the reversible sodiation/desodiation transformation at high current densities.

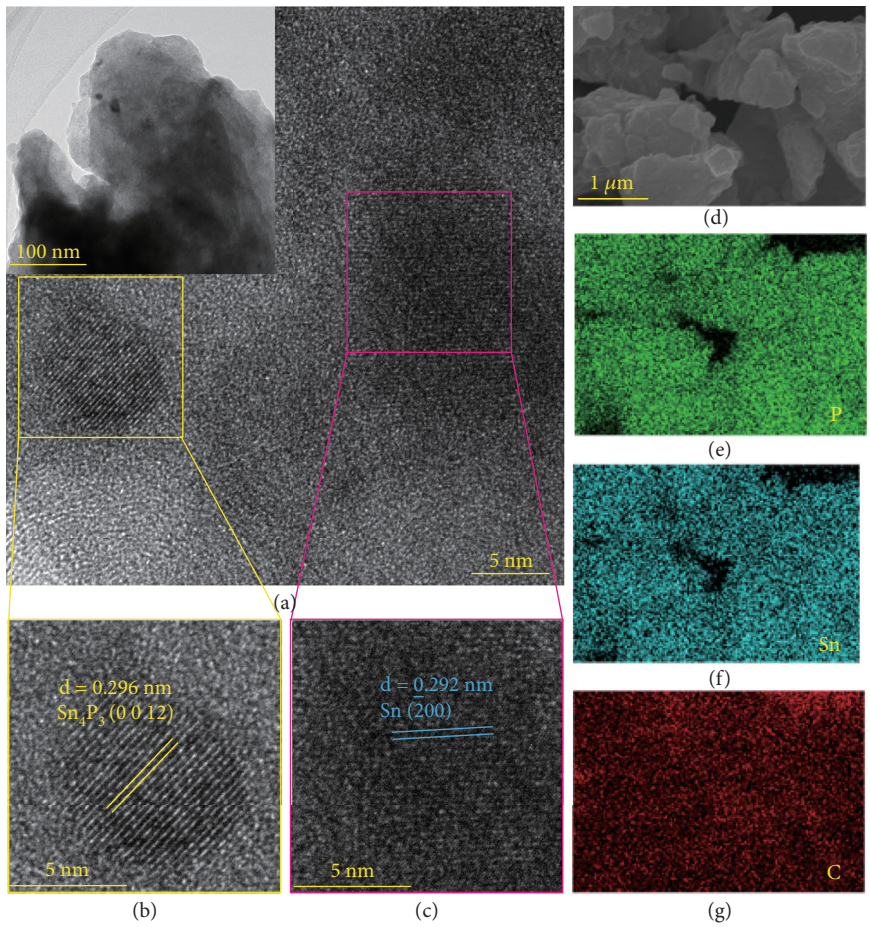

Figure 3: (a) Large-scale (inset) and HRTEM images of the representative composite anode C3. (b, c) Enlarged images from the marked regions in (a), showing the coexistence of Sn_4P_3 (b) and Sn (c) crystallites. (d–g) EDS image (d) and elemental distribution maps of P (e), Sn (f), and C (g) in the marked region.

Figure 4(e) displays the long-cycle performance of C3 at 1000 mA g^{-1}. Aside from the 1st cycle, C3 can work stably in the NIBs, delivering discharge capacities of 673.9 and 422.3 mAh g^{-1} in the 2nd and 300th cycles, respectively. Moreover, the Coulombic efficiency of C3 reaches to above 99.5% from ~26th cycle, further suggesting the high reversibility of C3 as the NIB anode material. Figure S5 shows the surface morphologies of C3 before and after 300 cycles analyzed by SEM. In the fresh electrode, C3 was blended with polyacrylic acid binder and conductive super P. However, the cycled electrode was obviously coated with SEI layer and there was no obvious crack, suggesting the good electrochemical reversibility of C3. The promising cycle reversibility of C3 in NIBs indicates that the Sn_4P_3 as well as Sn crystal domains embedded inside an amorphous P/carbon matrix significantly improve the electrochemical stability. Table S1 shows the performance comparison of the phosphorus-based anode for NIBs published in recent years, among which C3 has advantages in initial Coulombic efficiency and capacity.

We further explored the electrochemical performance of full cells, which were assembled using C3 as the anode and $Na_3V_2(PO_4)_3$ as the cathode. The electrochemical behavior of $Na_3V_2(PO_4)_3$ was first investigated in half-cells as shown in Figure S6. In order to balance the capacity between the two electrodes in the full cell, the N/P (anode/cathode) ratio was set as 1.2. The full cell was measured in the voltage range of 2.0-4.0 V at a current density of 50 mA g^{-1} and delivered an initial charge and discharge capacity of 111.6 and 110.3 mAh g^{-1} (based on the mass of $Na_3V_2(PO_4)_3$), respectively, with an initial Coulombic efficiency of 98.8%. A discharge capacity of 107.8 mAh g^{-1} could be obtained after 50 cycles, corresponding to a capacity retention of 97.7%, suggesting the effectiveness of C3 as anode materials in full cells.

It is challenging to precisely probe the structural evolution of P-/Sn-based anode materials with poor long-range ordering upon electrochemical cycling by conventional diffraction and microscopy techniques [43]. For example, the representative C3 anode material showed no correlated signal except for the Cu foil in the *ex situ* XRD as shown in Figure S7. *Ex situ* XPS test result of the C3 anode is shown in Figure S8. It is observed that the P $2p_{1/2}$ (132.7 eV) and PO_x (136.5 eV) peak weaken during the discharge process to 0.01 V and increase during the charge to 3.0 V. Since XPS is surface sensitive and cannot provide bulk information about the structural evolution of the anode material, we further applied *ex situ* NMR to investigate C3

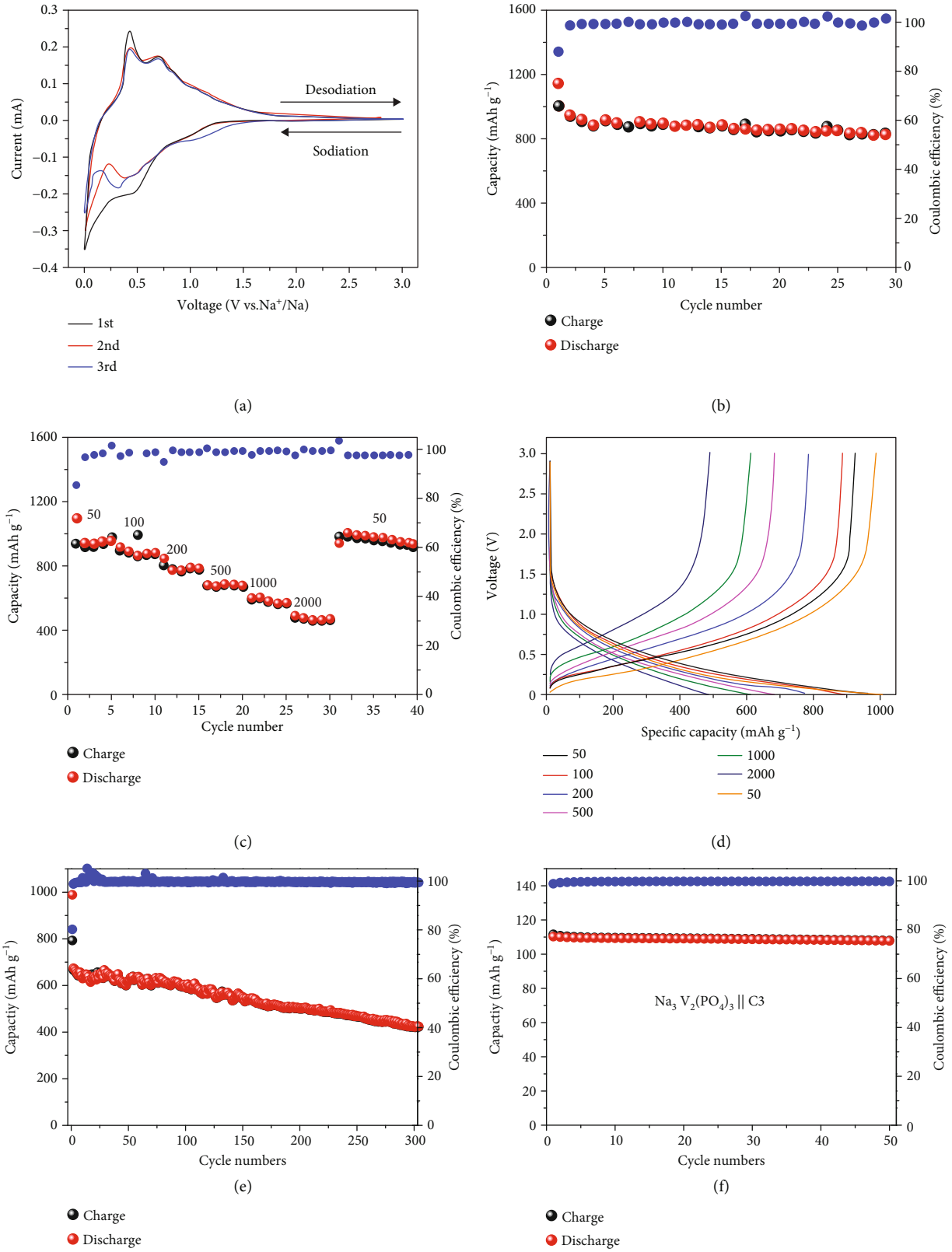

Figure 4: Electrochemical performance of the representative composite anode material C3 in NIBs. (a) CV curves of the initial three cycles of C3 at a scan rate of 0.1 mV s^{-1}. (b) Cycle performance of C3 at a current density of 200 mA g^{-1}. (c) Rate performance and Coulombic efficiency of C3 at various current densities from 50 mA g^{-1} to 2000 mA g^{-1}. (d) The corresponding typical charge/discharge voltage profiles in (c). (e) Long-cycle performance of C3 recorded at 1000 mA g^{-1}. (f) Cycle performance and Coulombic efficiency of the coin-type $Na_3V_2(PO_4)_3$||C3 full cell at 50 mA g^{-1}.

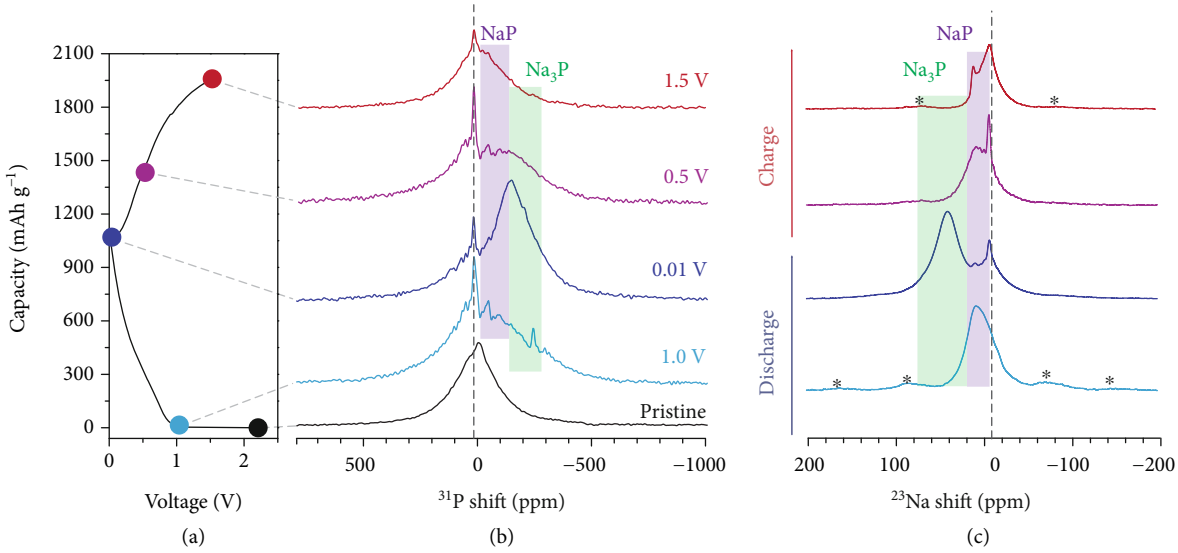

FIGURE 5: The electrochemical evolution of C3 probed by *ex situ* NMR investigations. (a) The charge/discharge curve with selected stages for *ex situ* NMR studies. (b) ^{31}P and (c) ^{23}Na MAS NMR spectra of C3 at various cycling stages marked in (a). The peaks labeled with asterisks are spinning sidebands.

at different electrochemical states. NMR is powerful to probe the local atomic environments and provide detailed structural information for noncrystalline materials [44, 45]. Well-resolved ^{23}Na and ^{31}P NMR spectra obtained under magic angle spinning (MAS) were taken to monitor the structural evolution of C3 during the sodiation/desodiation (Na_xP phases) processes at different charge/discharge stages (Figure 5). Figure 5(a) shows various charge/discharge states of C3 for the NMR investigation. As shown in Figure 5(b), the pristine C3 anode shows a single ^{31}P resonance centering at $\delta = 0$ ppm and spreading from −500 to 500 ppm. The broad linewidth and asymmetric peak reflect different chemical environments due to the noncrystalline nature [43]. For the electrode discharged to 1.0 V, a broad tail is observed at the right shoulder of the ^{31}P spectrum (Figure 5(b)), suggesting the formation of amorphous Na_xP [45–47]. The minor sharp peak at −245 ppm is probably originated from impurities during the sample treatment. Further discharge to 0.01 V, a variety of Na_xP alloys could be formed. Since the electrodes studied here are highly amorphous and have complicated environments, it is impractical to deconvolute these peaks, similar to the cycled NiP electrode [48]. However, it is assignable when referenced to the overlapping signals of crystalline NaP and Na_3P [47, 49]. The purple and green shadows represent NaP and Na_3P positions, respectively. Since the test powder is from the whole electrode plate, the voltage will rise back to ~0.2 V from 0.01 V when set rest after discharged to the final state. The phase of the final discharge state is composed of NaP and Na_3P. The sharp peak at 14 ppm likely originated from unreacted phosphorus which will decrease during the alloying reaction to form Na_xP.

The ^{23}Na NMR spectra of C3 at different cycling stages were further performed. Since the pristine C3 anode does not contain Na, the ^{23}Na NMR spectrum was not collected. After being discharged to 1.0 V, a peak at 6 ppm presenting in ^{23}Na NMR spectrum (Figure 5(c)) consolidates the formation of NaP. Upon further discharge to 0.01 V, the NaP peak almost disappeared and a new peak at 50 ppm noticeably appeared due to the generation of Na_3P [43, 46]. This further validates the analysis of the curve displayed in Figure 5(b) when discharged to 0.01 V. The sharp peak at −10 ppm in ^{23}Na NMR (Figure 5(c)) is attributed to the residual Na ions in the unwashed electrolyte.

A reversible evolution of C3 is observed from both ^{31}P and ^{23}Na NMR spectra upon subsequent charging. Refer to the spectra of 0.5 V and 1.5 V, resonances of ^{31}P show a downfield shift, whereas ^{23}Na move towards the upfield. The sodium is mostly extracted after one cycle to 1.5 V, which results in a dominant signal at −10 ppm for Na in the residual electrolyte. In sum, the amorphous sodiation/-desodiation of P-/Sn-based anode material is clearly characterized by the combination of solid-state ^{23}Na and ^{31}P NMR.

4. Discussion

In summary, a series of P-/Sn-based composite anode materials from different P/Sn ratios were prepared by the one-step high-energy ball milling method. With a rationalized P/Sn ratio, a configuration of Sn_4P_3 and Sn crystalline domains embedded inside an amorphous P/carbon matrix could be realized, combining the synergistic functions of crystalline structures and amorphous matrix. The composite structures were elucidated by a series of characterizations. Especially, PDF studies provide clear structure information not only about the formation of Sn_4P_3 and Sn crystal domains but also the quantitative information. The P-excess composites containing the highest amount of Sn_4P_3 delivered the best overall performance, with balanced capacities and cycle stabilities of above 422.3 mA h-g^{-1} for 300 cycles at 1000 mA g^{-1}. Combined with a $Na_3V_2(PO_4)_3$

cathode, a full cell delivered a discharge capacity of 110.3 mAh g^{-1} (based on the $Na_3V_2(PO_4)_3$) at 50 mA g^{-1} with a capacity retention of 97.7% after 50 cycles, suggesting the high effectiveness of the composite anode in full cells. The reaction mechanism of the optimal composite has been unraveled by ^{23}Na and ^{31}P NMR, showing a stepped sodiation process from NaP to Na_3P during the discharge of the composite. The study well adjusts and identifies the components and microstructures of P-/Sn-based anode materials, providing insights into the design of high-performance anode materials for NIBs.

Data Availability

The data and materials used to support the findings of this study are available from the corresponding author upon request.

Conflicts of Interest

The authors declare no conflict of interest regarding the publication of this article.

Authors' Contributions

H.J.Y. designed and supervised the study. B.X.C. and Y.B.Y. performed the material preparation, battery test, and characterizations. X.Z. and J.S. designed detailed experimental procedures. M.X.T made contributions on the ssNMR studies. B.X.C, X.Z., and H.J.Y wrote the paper. A.B.C provided administrative, technical, and supervisory support. All data are available in the main text or the supplementary materials. Baixu Chen and Yubo Yang contributed equally to this work.

Acknowledgments

This work was financially supported by the Beijing Natural Science Foundation (JQ19003), National Natural Science Foundation of China (Grants 21975006, 21875007, 22075007, U19A2018, and 51802009), and National Key R&D Program of China (Grant No. 2018YFB0104302). H. J. Yu appreciates the support from Beijing Youth Scholar program (PXM2021_014204_000023).

Supplementary Materials

Figure S1: SEM images of the composite C3 at magnification of (a) ×10 K and (b) ×100 K. Figure S2: cycle performance of Sn/P/C composites C1-C6 at 500 mA g^{-1}. Figure S3: (a) the GITT curves and (b) corresponding Na^+ diffusion coefficients of C3. Figure S4: cycle performance and Coulomb efficiency of super P carbon at 1000 mA g^{-1}. Figure S5: SEM observation of the surface of electrode: (a, b) before cycling and (c, d) after 300 cycles. Figure S6. (a) charge and discharge curves of $Na_3V_2(PO_4)_3$ and C3 in half cells are shown in blue and orange lines, respectively. (b) Cycle performance of $Na_3V_2(PO_4)_3$ at 50 mA g^{-1}. Figure S7: ex situ XRD patterns of C3 at different charge/discharge states. (a) The charge/discharge curve and selected stages of C3. (b) XRD patterns of C3 at different stages. Figure S8: ex situ XPS results of C3 at different charge/discharge states. (a) The charge/discharge curve and selected states of C3. (b) XPS results of C3 at different states. Table S1: a comparison of C3 composite with previously reported phosphorus-based anodes in SIBs. *(Supplementary Materials)*

References

[1] Q. Bai, L. Yang, H. Chen, and Y. Mo, "Computational studies of electrode materials in sodium-ion batteries," *Advanced Energy Materials*, vol. 8, no. 17, article 1702998, 2018.

[2] C. Delmas, "Sodium and sodium-ion batteries: 50 years of research," *Advanced Energy Materials*, vol. 8, no. 17, article 1703137, 2018.

[3] C. Mauger, M. Julien, M. Armand, and K. Zaghib, "Tribute to John B. Goodenough: from magnetism to rechargeable batteries," *Advanced Energy Materials*, vol. 11, no. 2, article 2000773, 2021.

[4] D. Vaalma, M. Buchholz, S. P. Weil, and S. Passerini, "A cost and resource analysis of sodium-ion batteries," *Nature Reviews Materials*, vol. 3, no. 4, pp. 1–11, 2018.

[5] H. Tan, D. Chen, X. Rui, and Y. Yu, "Peering into alloy anodes for sodium-ion batteries: current trends, challenges, and opportunities," *Advanced Functional Materials*, vol. 29, no. 14, article 1808745, 2019.

[6] J. Ni, L. Li, and J. Lu, "Phosphorus: an anode of choice for sodium-ion batteries," *ACS Energy Letters*, vol. 3, no. 5, pp. 1137–1144, 2018.

[7] Y. Kim, Y. Kim, A. Choi et al., "Tin phosphide as a promising anode material for Na-ion batteries," *Advanced Materials*, vol. 26, no. 24, pp. 4139–4144, 2014.

[8] T. Ramireddy, T. Xing, M. M. Rahman et al., "Phosphorus–carbon nanocomposite anodes for lithium-ion and sodium-ion batteries," *Journal of Materials Chemistry A*, vol. 3, no. 10, pp. 5572–5584, 2015.

[9] H. Ying and W.-Q. Han, "Metallic Sn-based anode materials: application in high-performance lithium-ion and sodium-ion Batteries," *Advanced Science*, vol. 4, no. 11, article 1700298, 2017.

[10] J. Saddique, X. Zhang, T. Wu et al., "Enhanced silicon diphosphide-carbon composite anode for long-cycle, high-efficient sodium ion batteries," *ACS Applied Energy Materials*, vol. 2, no. 3, pp. 2223–2229, 2019.

[11] H. Usui, Y. Domi, H. Nishida, K. Yamaguchi, R. Yamagami, and H. Sakaguchi, "Enhanced performance of Sn4P3Electrode cycled in ionic liquid electrolyte at intermediate temperature as Na-ion battery anode," *ChemistrySelect*, vol. 3, no. 29, pp. 8462–8467, 2018.

[12] J. Qian, Y. Xiong, Y. Cao, X. Ai, and H. Yang, "Synergistic Na-storage reactions in Sn_4P_3 as a high-capacity, cycle-stable anode of Na-ion batteries," *Nano Letters.*, vol. 14, no. 4, pp. 1865–1869, 2014.

[13] S. C. Jung, J. H. Choi, and Y. K. Han, "The origin of excellent rate and cycle performance of Sn_4P_3 binary electrodes for sodium-ion batteries," *Journal of Materials Chemistry A*, vol. 6, no. 4, pp. 1772–1779, 2018.

[14] J. Saddique, X. Zhang, T. Wu et al., "Sn_4P_3-induced crystalline/amorphous composite structures for enhanced sodium-ion battery anodes," *Journal of Materials Science & Technology*, vol. 55, pp. 73–80, 2020.

[15] W. Zhao, X. Ma, L. Gao, Y. Li, G. Wang, and Q. Sun, "Engineering carbon-nanochain concatenated hollow Sn_4P_3 nanospheres architectures as ultrastable and high-rate anode materials for sodium ion batteries," *Carbon*, vol. 167, pp. 736–745, 2020.

[16] L. Ran, B. Luo, I. R. Gentle et al., "Biomimetic Sn_4P_3 anchored on carbon nanotubes as an anode for high-performance sodium-ion batteries," *ACS Nano*, vol. 14, no. 7, pp. 8826–8837, 2020.

[17] Y. Pan, C. Jin, M. Zhao et al., "Mesoporous Sn_4P_3-graphene aerogel composite as a high-performance anode in sodium ion batteries," *Applied Surface Science*, vol. 475, pp. 12–19, 2019.

[18] J. Cui, S. Yao, and J. Kim, "Recent progress in rational design of anode materials for high-performance Na- ion batteries," *Energy Storage Materials*, vol. 7, pp. 64–114, 2017.

[19] T. Palaniselvam, C. Mukundan, I. Hasa et al., "Assessment on the use of high capacity "Sn_4P_3"/NHC composite electrodes for sodium-ion batteries with ether and carbonate electrolytes," *Advanced Functional Materials*, vol. 30, no. 42, article 2004798, 2020.

[20] W. Wang, J. Zhang, D. Y. W. Yu, and Q. Li, "Improving the cycling stability of Sn_4P_3 anode for sodium-ion battery," *Journal of Power Sources*, vol. 364, pp. 420–425, 2017.

[21] J. Liu, P. Kopold, C. Wu, P. A. van Aken, J. Maier, and Y. Yu, "Uniform yolk–shell Sn_4P_3@C nanospheres as high-capacity and cycle-stable anode materials for sodium-ion batteries," *Energy & Environmental Science*, vol. 8, no. 12, pp. 3531–3538, 2015.

[22] L. Ma, P. Yan, S. Wu, G. Zhu, and Y. Shen, "Engineering tin phosphides@carbon yolk–shell nanocube structures as a highly stable anode material for sodium-ion batteries," *Journal of Materials Chemistry A*, vol. 5, no. 32, pp. 16994–17000, 2017.

[23] Y. Pan, C. Jin, M. Zhao et al., "Conformal hollow carbon sphere coated on Sn4P3Microspheres as high-rate and cycle-stable anode materials with superior sodium storage capability," *ACS Applied Energy Materials*, vol. 2, no. 3, pp. 1756–1764, 2019.

[24] Y. Pan, C. Jin, M. Zhao, Q. Jia, M. J. Chang, and M. Jia, "Dopamine-derived N-doped carbon encapsulating hollow Sn_4P_3 microspheres as anode materials with superior sodium storage performance," *Journal of Alloys and Compounds*, vol. 769, pp. 45–52, 2018.

[25] Q. L. Lan and Q. Li, "Sn_4P_3/SbSn nanocomposites for anode application in sodium-ion batteries," *ChemElectroChem*, vol. 5, no. 17, pp. 2383–2386, 2018.

[26] Y. Xu, B. Peng, and F. M. Mulder, "A high-rate and ultrastable sodium ion anode based on a novel Sn_4P_3-P@graphene nanocomposite," *Advanced Energy Materials*, vol. 8, no. 3, article 1701847, 2018.

[27] J. Zhang, W. Wang, and B. Li, "Enabling high sodium storage performance of micron-sized Sn_4P_3 anode via diglyme-derived solid electrolyte interphase," *Chemical Engineering Journal*, vol. 392, article 123810, 2020.

[28] Y. Usui, K. Domi, M. Fujiwara et al., "Charge–discharge properties of a Sn4P3Negative electrode in ionic liquid electrolyte for Na-ion batteries," *ACS Energy Letters*, vol. 2, no. 5, pp. 1139–1143, 2017.

[29] P. K. Allan, J. M. Griffin, A. Darwiche et al., "Tracking sodium-antimonide phase transformations in sodium-ion anodes: insights from operando pair distribution function analysis and solid-state NMR spectroscopy," *Journal of the American Chemical Society*, vol. 138, no. 7, pp. 2352–2365, 2016.

[30] M. Key, J.-M. Morcrette, C. Tarascon, and P. Grey, "Pair distribution function analysis and solid state NMR studies of silicon electrodes for lithium ion batteries: understanding the (de)lithiation mechanisms," *Journal of the American Chemical Society*, vol. 133, no. 3, pp. 503–512, 2011.

[31] Y. Ma, P. Garcia, J. Lechelle et al., "Characterization of oxygen defect clusters in UO_{2+x} using neutron scattering and PDF analysis," *Inorganic Chemistry*, vol. 57, no. 12, pp. 7064–7076, 2018.

[32] S. Ortatatli, J. Knossalla, F. Schuth, and C. Weidenthaler, "Monitoring the formation of PtNi nanoalloys supported on hollow graphitic spheres using in situ pair distribution function analysis," *Physical. Chemistry Chemical Physics*, vol. 20, no. 13, pp. 8466–8474, 2018.

[33] S. Shiotani, K. Ohara, H. Tsukasaki, S. Mori, and R. Kanno, "Pair distribution function analysis of sulfide glassy electrolytes for all- solid-state batteries: Understanding the improvement of ionic conductivity under annealing condition," *Scientific Reports*, vol. 7, no. 1, pp. 6972–6977, 2017.

[34] J. M. Stratford, M. Mayo, P. K. Allan et al., "Investigating sodium storage mechanisms in tin anodes: a combined pair distribution function analysis, density functional theory, and solid-state NMR approach," *Journal of the American Chemical Society*, vol. 139, no. 21, pp. 7273–7286, 2017.

[35] L. Farrow, P. Juhas, J. W. Liu et al., "PDFfit2 and PDFgui: computer programs for studying nanostructure in crystals," *Journal of Physics: Condensed Matter*, vol. 19, no. 33, article 335219, 2007.

[36] P. Juhás, T. Davis, C. L. Farrow, and S. J. L. Billinge, "PDFgetX3: a rapid and highly automatable program for processing powder diffraction data into total scattering pair distribution functions," *Journal of Applied Crystallography*, vol. 46, no. 2, pp. 560–566, 2013.

[37] S. Hammersley, M. Svensson, A. Hanfland, D. H. Fitch, and D. Hausermann, "Two-dimensional detector software: from real detector to idealised image or two-theta scan," *High Pressure Research*, vol. 14, no. 4-6, pp. 235–248, 1996.

[38] J. Kim, H. Nakamura, Y. Shao et al., "Local structural evolution of mechanically alloyed $Mg_{50}Co_{50}$ using atomic pair distribution function analysis," *The Journal of Physical Chemistry C*, vol. 115, no. 15, pp. 7723–7728, 2011.

[39] Z. Tian, G. Li, Z. Feng et al., "Stable, high-performance, dendrite-free, seawater-based aqueous batteries," *Nature Communications*, vol. 12, no. 237, pp. 1–12, 2021.

[40] G. Wang, M. Aubin, A. Mehta et al., "Stabilization of Sn anode through structural reconstruction of a Cu–Sn intermetallic coating layer," *Advanced Materials*, vol. 32, no. 42, article 2003684, 2020.

[41] L. Ran, I. Gentle, T. Lin et al., "Sn_4P_3@Porous carbon nanofiber as a self-supported anode for sodium-ion batteries," *Journal of Power Sources*, vol. 461, article 228116, 2020.

[42] Q. Li, Z. Li, Z. Zhang et al., "Low-temperature solution-based phosphorization reaction route to Sn_4P_3/reduced graphene oxide nanohybrids as anodes for sodium ion batteries," *Advanced Energy Materials*, vol. 6, no. 15, article 1600376, 2016.

[43] L. E. Marbella, M. L. Evans, M. F. Groh et al., "Sodiation and desodiation via helical phosphorus intermediates in high-

capacity anodes for sodium-ion batteries," *Journal of the American Chemical Society*, vol. 140, no. 25, pp. 7994–8004, 2018.

[44] J. Bekaert, S. Bernardi, L. Boyanov, M.-L. Monconduit, M. L. Doublet, and M. Ménétrier, "Direct correlation between the31P MAS NMR response and the electronic structure of some transition metal phosphides," *Journal of Physical Chemistry C*, vol. 112, no. 51, pp. 20481–20490, 2008.

[45] M. Mayo, K. J. Griffith, C. J. Pickard, and A. J. Morris, "Ab initio study of phosphorus anodes for lithium- and sodium-ion batteries," *Chemistry of Materials*, vol. 28, no. 7, pp. 2011–2021, 2016.

[46] R. Morita, K. Gotoh, M. Dahbi et al., "States of thermochemically or electrochemically synthesized Na_xP_y compounds analyzed by solid state ^{23}Na and ^{31}P nuclear magnetic resonance with theoretical calculation," *Journal of Power Sources*, vol. 413, pp. 418–424, 2019.

[47] L. Xu, Z. Chen, G. M. Zhong et al., "Nanostructured black phosphorus/Ketjenblack–multiwalled carbon nanotubes composite as high performance anode material for sodium-ion batteries," *Nano Letters*, vol. 16, no. 6, pp. 3955–3965, 2016.

[48] X. Feng, M. Tang, S. O'Neill, and Y.-Y. Hu, "In situ synthesis and in operando NMR studies of a high-performance Ni_5P_4-nanosheet anode," *Journal of Materials Chemistry A*, vol. 6, no. 44, pp. 22240–22247, 2018.

[49] H. Jin, Z. Wang, D.-S. Qi et al., "A black phosphorus-graphite composite anode for Li-/Na-/K-ion batteries," *Angewandte Chemie International Edition*, vol. 59, no. 6, pp. 2318–2322, 2020.